Post-Print

When citing this work, cite the original published paper.

Numerical Investigation of Ice Formation on a Wing with Leading Edge Tubercles

Lorenzo Beretta*, Myles Morelli[†], Alberto Guardone [‡] and Giuseppe Quaranta[§]
Department of Aerospace Science & Technology, Politecnico di Milano, Milan, 20156, Italy

This work numerically investigates the influence of sinusoidal leading-edge characteristics, often described as *wavy* leading edge wings or wings with *tubercles*, on aircraft icing. Initially, the flow prediction of clean wavy wings is compared to experimental data for model validation. A series of test cases based on the experimental geometry is subsequently established with varying wave amplitudes and lengths. The icing assessment is conducted numerically using the three-dimensional PoliMIce ice accretion toolkit. Firstly, the influence of the three-dimensional flow behaviour on the collection efficiency is evaluated. The simulations demonstrate that wavy leading edges with shorter wave lengths and higher wave amplitudes increase the localised impingement of super-cooled water droplets during impact. Secondly the influence of the wavy leading edge profile on the ice shapes is assessed for both the rime and glaze ice regime. The results show that the maximum ice thickness is in the vicinity of the wave peaks and troughs meanwhile the mid-sections of the waves have significantly lower levels of ice accretion. The future perspective of this work is to assess the potential for improving the efficiency of anti-icing and de-icing systems using wavy leading-edges.

Nomenclature

Symbols

A	=	leading edge sine amplitude
c	=	chord length
C_D	=	drag coefficient
C_L	=	lift coefficient
C_M	=	moment coefficient
F_s	=	safety factor
p	=	static pressure

---

*Graduate Student, email address: lorenzo5.beretta@mail.polimi.it
[†]Post-Doctoral Researcher, email address: mylescarlo.morelli@polimi.it
[‡]Full Professor, email address: alberto.guardone@polimi.it
[§]Full Professor, email address: giuseppe.quaranta@polimi.it

q	=	order of convergence
$\mathfrak{R}$	=	grid refinement ratio
Re	=	Reynolds number
s	=	non-dimensional curvilinear coordinate
T	=	environmental temperature
U_∞	=	freestream velocity

Greek Letters

β	=	collection efficiency
$\epsilon_{i+1,i}$	=	relative error between computational grids $i+1$ and i
ρ	=	density

Abbreviations

AoA	=	angle of attack
GCI	=	grid convergence index
LWC	=	liquid water content
MVD	=	median volume diameter
RBF	=	radial basis function
WL	=	leading edge sine wavelength

I. Introduction

Ice accretion is a major issue for aircraft flying in cold wet air, since super-cooled water particles may freeze on the aerodynamic surfaces, provoking a series of detrimental effects which threaten flight safety [1]. The accretion of ice leads to a deterioration in aerodynamic performance due to increased drag and decreased lift. Moreover, wings can experience early onset stall as ice increases the likelihood of flow separation. Additionally, ice may lead to loss of control or reduce the effectiveness of control surfaces as ice accretes on ailerons, elevators, and rudders [2]. As a result, ice further impacts the handling qualities of aircraft [3].

Additional concerns include the possible interaction with engines [4]. Ice has the potential to form on the first stator and rotor stages and may even lead to significant power losses. The formation of ice on high speed rotating components can cause ice shedding events generating unbalancing phenomena. To that end, shed ice may even damage compressor components. Finally, the formation of ice near the engine's intake can alter the air inflow in the inlet manifold. Furthermore, the formation of ice on external sensors such as pitot tubes is particularly dangerous as it can

affect the accuracy of measurements. The formation of ice on pitot tubes has led to a series of high profile and even catastrophic accidents [5].

It is evident from the aforementioned examples that ice accretion may severely affect both performances and safety, thus being one of the primary concerns for aircraft which operate in such adverse climate conditions. Stemming from these concerns, researchers have developed an increasing awareness of the icing phenomenon through experimental and numerical studies to predict and limit the effects of icing. While flight tests and wind tunnel experiments have been extensively used throughout the design and certification of aircraft, they are not without limitations. Flight tests rely on forecasting highly uncertain meteorological icing events and wind tunnel experiments are often limited to icing sub-scale models of isolated components. Recently, numerical techniques have been harnessed for the early analysis of icing and to complement flight tests and wind tunnel experiments.

Innovative designs to improve the efficiency and effectiveness of ice protection systems are continuously being developed by industry and academia. The employment of a sinusoidal leading edge for reducing ice accretion is suggested in a patent from Airbus [6], where it is hypothesized that ice may form only on isolated portions of the wing. It is thought that the major advantage of using a wavy leading edge is to alter the distribution of the collected water droplets on the wing to focused regions where an ice protection system is located. Since the leading edge is constituted by a repetition of peaks and troughs, which generate a certain amount of spanwise flow, super-cooled water droplets may be subject to increasing aerodynamic forces in oblique regions of the leading edge and only a reduced portion might impact there. It is then expected that ice structures will form mainly in the proximity of stagnation points, located downwards peaks and troughs of the leading edge, while they will be reduced on the remaining portions of the wing. A potential reduction of ice structures would provoke a series of positive effects, varying from a lower loss of performance to the reduction in thermal energy provided by an anti- or de-icing system. Also, the preferred formation of ice on isolated portions of the wing surface might be beneficial from a safety point of view too, possibly reducing the extent of stall or the occurrence of ice shedding phenomena.

This work aims to study the mechanisms behind the ice accretion on wavy leading edges to understand possible practical advantages in their employment to limit the ice formation. The use of numerical simulations is exploited for this qualitative preliminary assessment to the potential of a patented idea from Airbus. The paper aims to answer the question if there is a sufficient positive trend to justify experimental testing of wavy leading edge wing configurations in icing conditions.

The organisation of the remaining work is as follows: Section II discusses and summarizes relevant studies by the scientific community related to wavy leading edges; Section III discusses the latest ice prediction capabilities; Section IV introduces the PoliMIce framework which is utilized for the numerical analysis of ice accretion on wavy leading edges; Section V examines the numerical flow of clean wavy leading edges with experimental measurements before an icing analysis; Section VI assesses the main results including the collection efficiency and ice accretion; Section VII

summarizes the key conclusions and highlights the main differences between the wavy wing and the straight wing icing.

II. Wavy Leading Edges

The characteristic sinusoidal leading edge shape is often referred to in the literature as either *wavy* leading edge wings or wings with *tubercles*.

Interest shown by the aeronautical community in the use of sinusoidal leading edge wings stems from experimental evidence suggesting that the characteristic leading edge shape deeply alters the stall mechanism. Instead of having a sharp loss of performances concentrated at a specific angle of attack, the stall is smoothed over a much wider range, thus avoiding the characteristic abrupt loss of lift [7–14]. In some cases, stall is eliminated and performances remain almost constant increasing the incidence of the wing.

The aerodynamic concept of wavy leading edges is inspired by the animal kingdom. The pectoral flippers of humpback whales are a classic example of wavy edge structures in nature. It has been suggested that tubercles work as lift-enhancer devices, modifying the flow field in such a way to permit water to remain attached for a larger range of angles of attack, thus allowing whales to perform more demanding turning maneuvers and improve their hunting skills [15].

A wide variety of experiments have been conducted on wings with leading edges that mimics the wavy characteristics of humpback whale flippers. As summarised by Gopinathan and Rose [16], the vast majority of both wind tunnel tests and numerical investigations available in state-of-the-art literature are carried at medium-low Reynolds numbers similar to that of the humpback whale flipper, generally not exceeding $Re = 10^6$, and analysis focuses on variations in leading edge geometry and effect of the Reynolds number.

The geometry of a wavy wing is primarily governed by sine's amplitude and wavelength and various authors agree on the major role these parameters have in altering the flow field, leading to a different stall mechanism compared to the classic one on straight wings [7, 8]. In general it has been found that higher amplitudes tend to smooth stall, meaning that the drop in the lift coefficient is spread over a much larger range of angles of attack, rather than being concentrated on a specific value and leading to an abrupt loss of performance. On the other hand, smaller amplitudes achieve higher maximum values of C_L, but they present a certain amount of abrupt loss of lift, still of a reduced extent if compared to the straight leading edge wings counterpart. Through reducing the wavelength, airfoil performances improve in terms of both maximum lift and stall characteristics. However, after a limit value of the wavelength, improvements cease to exist.

In general, the aerodynamic performances of a wavy wing are reduced when the angle of attack is in the pre-stall range. Conversely, they are higher when angles of attack are past the straight wing's stall point. The extent of these modifications is regulated by the wave amplitude and length.

The flow mechanism behind the differences in performance is described by several authors. The three-dimensional sinusoidal leading edge deviates the incoming flow from peaks to troughs, see Fig. 1. The so-called spanwise flow

produces a strong acceleration in the trough regions, leading to an enhanced suction there [17]. On the other hand, the flow behind peaks transported away by the spanwise flow is replaced by high momentum fluid from the above, which re-energise the boundary layer, locally reducing suction and ultimately delaying separation [18]. Also, this phenomenon originates streamwise vortices similar to those of delta wings [19].

The differences in pressure gradient behind peaks and troughs modify the stall behaviour of the wing: when the angle of attack is increased, flow separation initially occurs only downstream trough regions, while the flow remains perfectly attached behind peaks. On wavy wings, an alternating pattern of attached-detached flow is then established, which is the cause for a smoothed stall and differences in performance compared to a straight wing.

Additional insight is provided in [20], where it is investigated the effect of the Reynolds number on lift and drag performances of wavy wings. Results show how for very low Reynolds numbers wavy wings may be superior to straight ones in terms of both lift and drag coefficients for the whole range of angles of attack from zero to stall angle, in addition to the already mentioned improved post-stall characteristics.
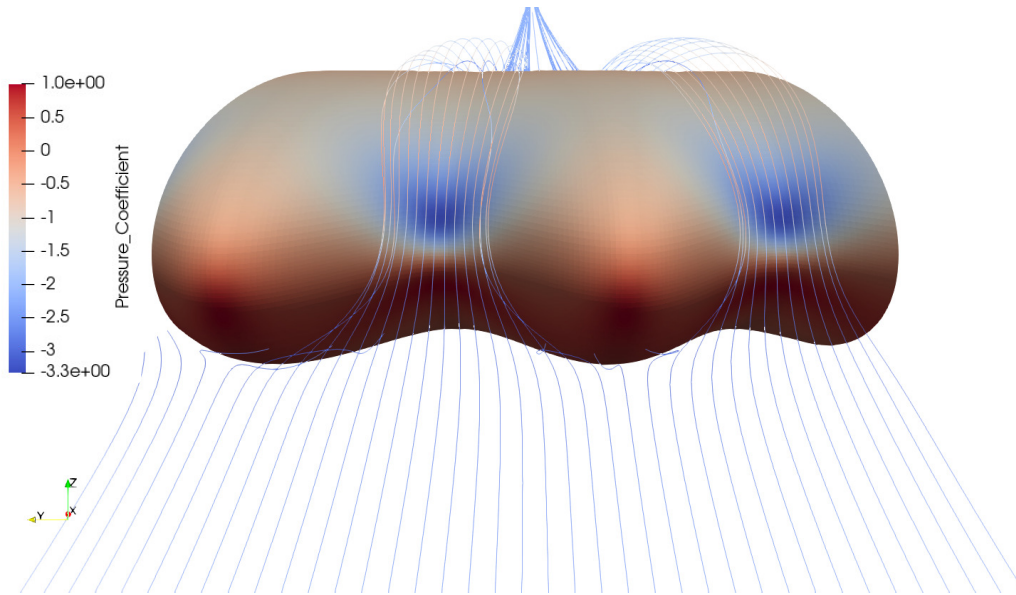
Fig. 1   Streamlines over a wing with a wavy leading edge and the surface pressure distribution.

As a consequence of these findings, possible uses of these aerodynamic surfaces include all applications that require to operate past the stall point or where the Reynolds number is inherently low. Belonging to the first category are wind turbines blades, where power generation at lower wind speeds is challenging, boat centerboards, rudders and in general all control devices possibly subject to stall. Regarding the second category, examples of possible employments of wavy wings concern unmanned aerial vehicles or drones, because of their reduced dimensions.

III. Ice Prediction

The simulation of ice accretion involves solving a multi-phase problem encompassing the flow of air, water droplets and ice. The first step is to compute the flow around the surface of interest. The second step is associated with determining the rate at which water droplets impact, while the final step is represented by the rate at which the impacted water freezes and forms an ice structure. This process is typically solved iteratively with the mesh being updated at each sub-iteration.

In 2021, the 1st Ice Prediction Workshop (IPW) was established in conjunction with the AIAA AVIATION Forum. The objective of the IPW was to: (1) compare ice shapes between two- and three-dimensional codes with experimental ice shapes; and (2) establish a sound baseline of current simulation capabilities [21]. The IPW brought together industry and academia to provide a collaborative platform for cross-code model comparison and verification. The results presented at the IPW highlighted that while there is relatively good agreement between codes for rime ice geometries, there remains significant scope for improvement on more complex glaze ice geometries and in particular for three-dimensional ice shapes. Additionally, it was observed that while codes are able to predict Appendix-C conditions, the presence of super-cooled-large droplets (SLD) in Appendix-O conditions requires further investigating. In particular the influence of wall interaction models is an area which can be improved.

Significant advances have been made over recent years to improve the accuracy and fidelity of numerical ice prediction capabilities. The subsequent literature review focuses on improvements in three-dimensional, multi-step ice prediction capabilities due to this be inherently important for the prediction of ice accretion on wavy leading edges. Chen and Zhao introduced a three-dimensional approach for the simulation of rotorcraft icing to address concerns over using two-dimensional icing approaches for highly three-dimensional problems [22]. In their approach they used a grid regeneration technique to account for the three-dimensional evolving ice boundary. Their work utilized an Eulerian particle tracking approach with a shadow zone dispersion model for computing the droplet trajectories and collection efficiency on the moving rotor blades [23]. Lavoie et al. [24] introduced an immersed boundary approach combined with level set for updating the moving ice boundary during multi-step icing simulations. Their work identified the benefits of an immersed boundary approach over the usual body-fitted approach for in-flight icing simulations. The immersed boundary approach is able to account for complex glaze ice shapes particularly well. However the approach was only demonstrated for two-dimensional problems. The ice roughness is typically modeled as constant over the surface by many numerical models. Szilder and Lozowski introduced a morphogenetic modeling approach to improve the prediction of complex three-dimensional ice structures under rime and glaze ice regimes [25]. The morphogenetic model is unique in that it has the inherent ability to simulate rough and discontinuous ice structures due to the model's discrete formulation. Their work showed that the morphogenetically simulated accretions exhibit three-dimensional features similar to experimental icing shapes. The reliability and accuracy of the three-dimensional, unsteady modelling techniques is also of genuine concern due to a high level of uncertainty in aircraft icing. Gori et al. investigated

the uncertainties of in-flight icing conditions under Appendix-C icing conditions [26]. Their work investigated the influence of parameters including the AoA, MVD, and LWC on the final ice shapes. In the rime ice accretion regime, the variability of the predicted thickness was found to be largely associated to the cloud MVD and airfoil AoA. In contrast, in the glaze ice regime, the LWC and MVD were shown to dominate with the influence of the AoA being negligible.

IV. PoliMIce Framework

In this work the PoliMIce framework [27] is utilized and is composed of different software, each of which solves a dedicated step of the simulation. The fundamental hypothesis of one-way coupled flow means that steps are sequentially solved to determine the ice thickness. This process is solved in an iterative approach in what is known as multi-step ice accretion as shown in Fig.2. PoliMIce has been developed with highly three-dimensional and unsteady problems in mind such as rotorcraft [28–30], making it suitable for the analysis of wavy leading edge icing. The individual solvers which are utilized for the multi-step icing simulation are hereinafter briefly outlined.
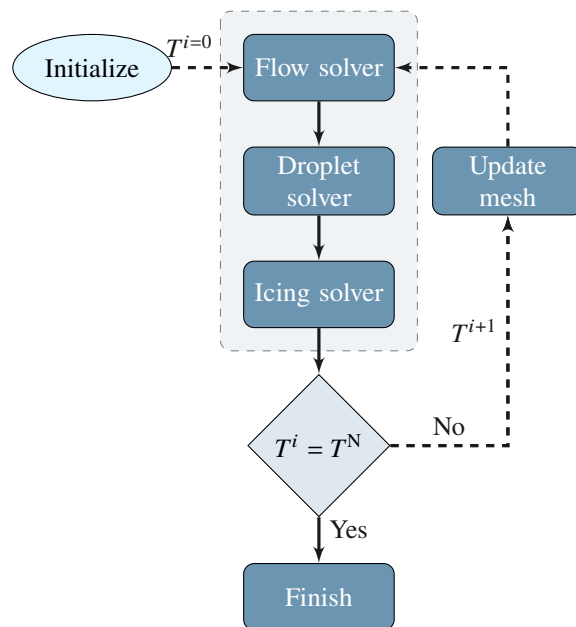
Fig. 2   Schematic of a multi-step icing simulation.

The SU2 software suite [31] is an open-source toolkit written in C++ and Python created for multi-physics simulation and design. It is built specifically for the analysis of partial differential equations (PDEs) and PDE-constrained optimization problems on unstructured meshes with state-of-the-art methods and algorithms and is particularly well suited for aerodynamic shape design. The Finite volume method (FVM) is applied on arbitrary unstructured meshes using a standard edge-based data structure on a dual grid with control volumes constructed using a median-dual, vertex-based scheme. The core of the suite is a Reynolds-averaged Navier-Stokes (RANS) solver which is used in this study in tandem with the Spalart–Allmaras (SA) turbulence model.

Trajectories of super-cooled water droplets are calculated as well as the resulting water distribution on the surface using the Lagrangian PoliDrop solver[32]. The droplet solver numerically integrates in time the equations of motion of every single particle, using a standard Forward Euler algorithm. The collection efficiency, β, is the fundamental outcome of this step. This quantity is defined as the ratio between the droplets stream tube area at wing surface and the area at farfield, it can be regarded as a non-dimensional density of water droplet impacts. The collection efficiency plays a major role in the present application since it may be the main factor of an altered ice distribution over the wing surface.

The PoliMIce solver [27] is used for computing the ice thickness and shape. The rate and amount of ice accretion on an unheated surface depends on several parameters including the flight speed, surface temperature, the liquid water concentration, LWC, and the size of water droplets in the cloud, represented by the Median Volume Diameter, MVD. These parameters influence both the amount of ice accretion and the resultant typology of ice structures, i.e. rime or glaze ice. On each surface cell a one-dimensional accretion problem, enforcing mass and heat balances, is solved in the direction normal to the surface. Several physical models, describing the phenomenon, are implemented in PoliMIce including the well-known Myers [33] and state-of-the-art ice formation models based on the local, exact solution of the unsteady Stefan problem for the temperature profiles within the ice layer in glaze conditions [34]. As a result, after the desired exposure time, the ice layer thickness is calculated and the new positions of surface points are computed.

Radial Basis Function (RBF) mesh deformation [35] is used to update mesh after each step of the icing simulation. The new positions of all volume points in the grid are recomputed starting from the new position of the surface points. Multi-level greedy surface point selection data reduction schemes are utilized to efficiently deform the three-dimensional mesh.

A. Model Validation

To the authors best knowledge there are no experimental measurements for the validation of the ice prediction on wing with wavy leading edges. For this reason, several well-known fixed-wing experimental test cases have been selected for preliminary validation of the three-dimensional ice accretion models. The test cases are part of the AIAA Ice Prediction Workshop. The first experimental test case selected is for the validation of the collection efficiency model on a full-scale horizontal swept tail [36]. The second test case selected is for the validation of the predicted ice shapes from Lee et al. [37].
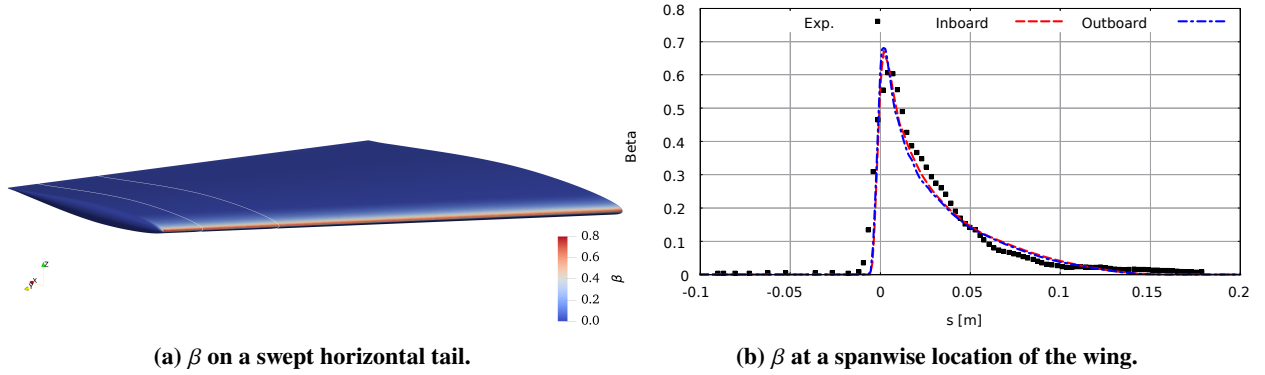
1. Collection Efficiency

The extensive experimental database from Papadakis et al. [36] is used for the validation of water droplet impingement models. The experimental tests were conducted in the NASA Glenn Icing Research Tunnel (IRT) on a range of configurations and included measurements of the flow and droplet impingement. The configuration selected here is the outboard portion of a full-scale horizontal swept tail from a general business jet with a NACA 64A008 profile.

8

The operating conditions are shown in Table 1 and are representative of Appendix C conditions.

Table 1   Collection Efficiency Conditions taken from Ref. [36].

Mach	AoA	Pressure	Temp	MVD	Re	Chord
[–]	[°]	[Pa]	[K]	[g/m^3]	[–]	[in]
0.23	6.0	83,025	291.2	21	5.03×10^6	37.65

The water droplet impingement model is compared with the experimental recordings in Fig. 3. Impingement data was again obtained at two spanwise stations as shown in Fig. 3a. Only the experimental data at the inboard station is displayed for clarity due to high similarity in the measurements. The prediction of the collection efficiency on the swept horizontal tail is shown in Fig. 3b. The collection efficiency peak and droplet impingement limits are well represented.

(a) β on a swept horizontal tail.

(b) β at a spanwise location of the wing.

Fig. 3   NACA 64A008 swept tail collection efficiency, β, with a MVD = 21μm compared to experimental data from Ref.[36].

2. Ice Accretion

The conditions from Lee et al. [37] correspond to streamwise rime icing conditions and glaze icing conditions which produce ice horns. The test conditions are displayed in Table 2.

Table 2   Icing Conditions taken from Ref. [37].

Mach	AoA	Temp	MVD	LWC	Re	Chord
[–]	[°]	[K]	[μm]	[g m^{-3}]	[–]	[in]
0.3	2.0	255.35, 271.25	30, 15	0.42, 0.81	3.5×10^6	18

The ice prediction results for the straight wing configuration are shown in Fig. 4. The two-dimensional simulation results are compared to the Maximum Combined Cross Section (MCCS) of the experimental ice scans from Lee et al. [37]. The first simulations are representative of the rime ice regime and are shown in Fig. 4a. The numerical prediction over predicts the ice thickness on the leading edge when compared to the MCCS. The second simulations are

representative of the glaze ice regime and are shown in Fig. 4b. The glaze ice regime produces distinctive double ice horns which the numerical predictions capture. The PoliMIce framework predicts complex two-dimensional ice shapes which exhibit strong similarities to the MCCS experimental measurements. Additionally, parameters which strongly influence the final ice shape are assessed. It shows that the mesh sensitivity and number of multi-step time intervals have a greater influence on glaze ice shapes. Both the mesh refinement and number of multi-step time intervals impact the size and angle of the ice horns.

(a) Rime ice accretion.

(b) Glaze ice accretion.
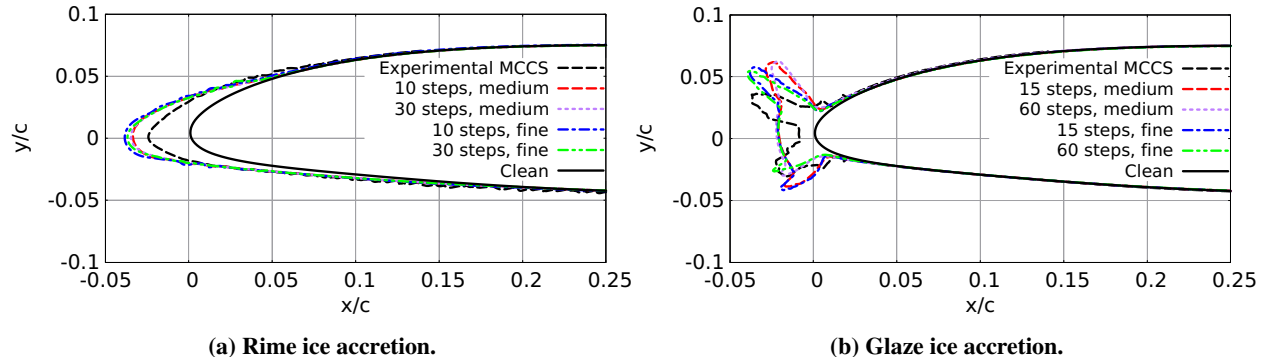
Fig. 4   Mesh and time step sensitivity analysis.

V. Clean Wavy Wing Validation

As the first phase, the flow around the clean sinusoidal wings is compared to wind tunnel experimental measurements for validation. To this end, numerical results using the SU2 solver are compared with experimental measurements from de Paula [11]. The wind tunnel experiments were performed at Re = 290000. Three modified sinusoidal leading edge geometries and a baseline straight leading edge are used. All geometries are based on a NACA 0012 profile with constant chord length. The three modified geometries are called A011WL040, A003WL040, and A003WL011 and the details are described in Table 3:

Table 3   Summary of wavy leading-edge geometry taken from de Paula [11].

Characteristics	Label	A[c]	WL[c]	A/WL ratio
NACA 0012 unmodified	BASELINE	–	–	–
Low A, Short WL	A003WL011	0.03	0.11	0.273
Low A, Long WL	A003WL040	0.03	0.40	0.075
High A, Long WL	A011WL040	0.11	0.40	0.275

The geometry of the sinusoidal wavy leading edges in Table 3 is defined by:

$$x = A \sin\left(\frac{2\pi}{\text{WL}}y\right) \tag{1}$$

10

where x is the local chord length and y is the spanwise location. The varying sinusoidal attributes of the wing are expressed by A which is the amplitude of the sinusoidal wave and WL which is the wave length. Subsequently, $A/$WL is the parametric ratio of the amplitude to the wavelength.

Radial Basis Function (RBF) mesh deformation techniques are used to account for the wavy leading edge. RBF mesh deformation techniques are robust and preserve high-quality mesh even during large deformations which are important for large wave lengths. The details of the RBF mesh deformation techniques used are discussed in Refs.[35] and [38]. In general, an interpolation function can be introduced as a method for describing the displacement of a set of nodes in space and can be approximated by a weighted sum of basis functions. The grids generated by RBF ensure an average best cell quality and discretization consistency among different geometries. The baseline and wavy computational grids are shown in Fig. 5.

As a common practice, a grid independence study was performed to assess the independence of numerical results from the domain discretization [39]. For the problem at hand, the Spalart-Allmaras turbulence model is adopted. Bas-Cakmakcioglu (BC) transition model is coupled with the SA model to compute the flowfield across the various geometries. The Bas-Cakmakcioglu transition model is qualified as an algebraic, or a zero-equation, model since it does not introduce any further equation in the underlying turbulence model to solve the RANS equations. The advantage in using an algebraic model relies in increasing simulation speed, since the number of equations to be solved (6 using SA-BC) is lower than when using more complex transition models. This is a characteristic that is very welcome when dealing with iterative large three-dimensional problems as in the present case. However, even if SA-BC provides aerodynamic coefficients that are closer to the experimental ones for the baseline configuration, it results in reduced convergence rate on wavy wings providing no accuracy benefit. The lack of an accuracy benefit for wavy wings is not unexpected, as the model relies on assumptions and simplifications, which are valid in a Blasius boundary layer and still acceptable only in applications where the pressure gradients are moderate. On the other hand, more complex transition models are excluded as well, as any possible accuracy benefit would be accompanied by a significantly increased computational time. Stemming from these considerations, it is ultimately decided to employ Spalart-Allmaras turbulence model alone, for all simulations and on all geometries. Integration in space is achieved employing the Jameson-Schmidt-Turkel scheme, that is a second-order accurate, central scheme.

The computational grid is a structured C-type, composed by hexahedral elements, and whose boundaries extend for 15 chords all around the profile: farfield boundary conditions are applied to the surfaces around the profile, the wing is modelled as a no-slip adiabatic wall and periodic boundary conditions are applied to the two side planes. The total number of elements for the finest mesh of a two-wavelengths profile is 3840000. The surface discretization has proven to be of utmost importance, and both the spanwise and chordwise directions have been refined until the number of surface elements is sufficient to predict the flow topology accurately. As a result, the wing surface is composed by 38400 quadrilaterals corresponding to 160 elements along the span and 240 along the chord for all sinusoidal configurations

11
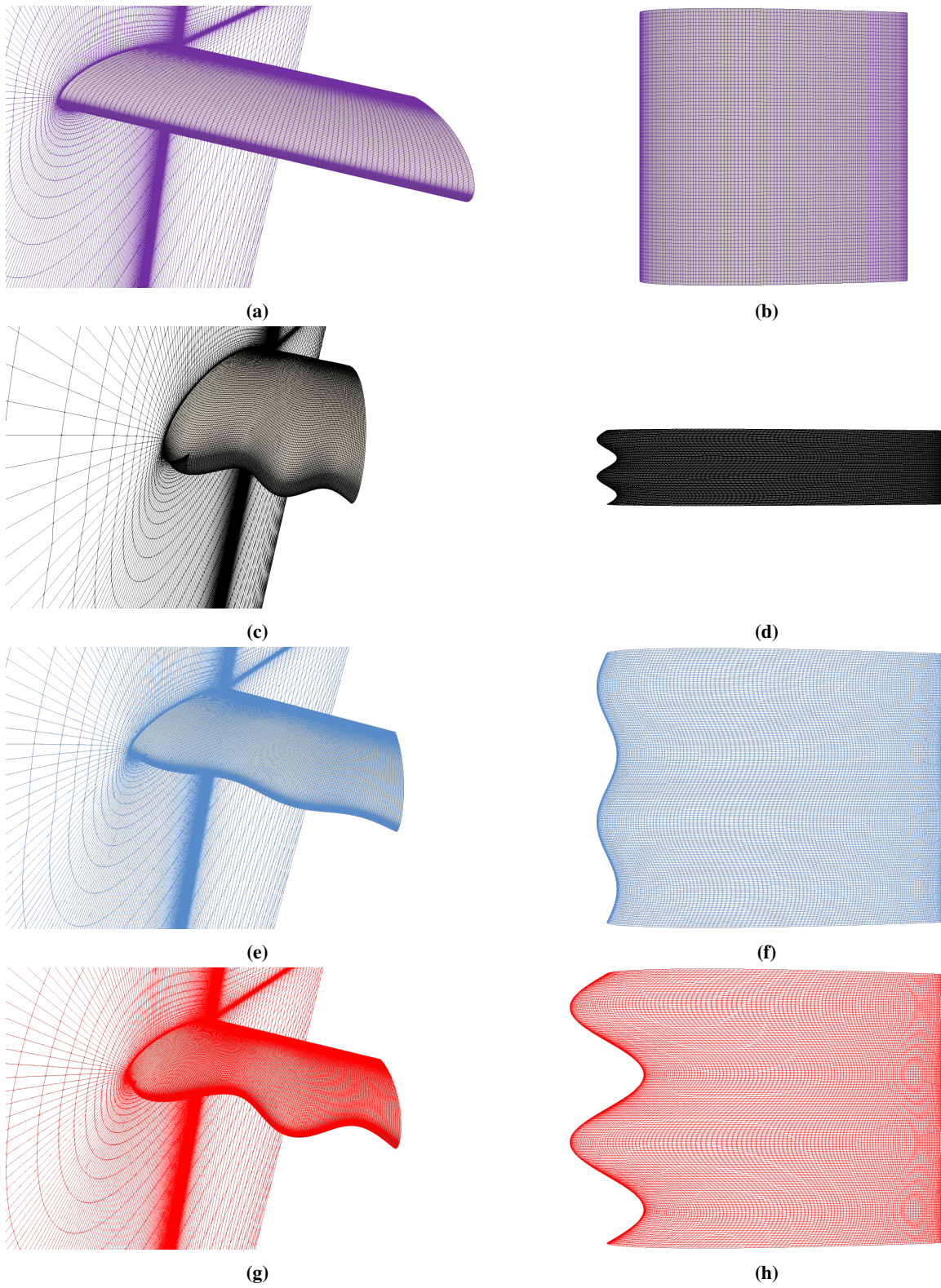
Fig. 5   Baseline and wavy wing computational grids. (a) Baseline 3D, (b) Baseline 2D, (c) A003WL011 3D, (d) A003WL011 2D, (e) A003WL040 3D, (f) A003WL040 2D, (g) A011WL040 3D, (h) A011WL040 2D.

and for the straight wing. The first layer of cells from the wall has a height $h = 2.5 \times 10^{-6}$ m, in order to provide a suitable value of $y^+ < 1$ at the wing surface. The elements of the subsequent external layers have approximately 120% the height of the neighbouring inner layer, to ensure a proper boundary layer discretization.

A series of four grids are generated, indexed 4 to 1, trending from coarse to fine. Each fine grid has approximately twice the elements of the coarse grid leading to a refinement ratio of $\mathfrak{R} \approx 2$. This means that each of the three orthogonal spatial directions is discretized using a number of elements that is $\sqrt[3]{2}$ times those used for the coarse grid. The study is reported for the sinusoidally deformed mesh $A = 0.11c, WL = 0.40c$ at a constant angle of attack $AoA = 5°$ and values of C_L, C_D and C_M are examined. The same study is made on the mesh with $A = 0.03c, WL = 0.11c$ at a constant angle of attack $AoA = 10°$, however the results qualitatively present the same trend and are not reported for brevity. Results of mesh refinement on the aerodynamic coefficients are reported in Table 4.

Table 4   Mesh refinement levels and corresponding aerodynamic coefficients.

Grid index	Number of elements	C_L	C_D	C_M
4	957600	0.392551	0.022992	-0.005681
3	1923264	0.462766	0.020063	-0.004059
2	3840000	0.499077	0.018182	-0.003630
1	7768112	0.503737	0.017668	-0.003451
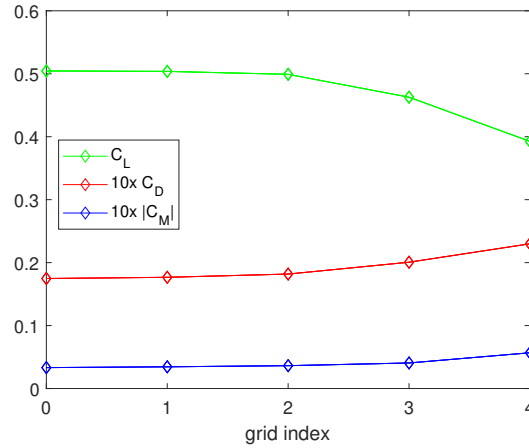
Fig. 6   Grid convergence analysis displaying the aerodynamic coefficients. Index 0 indicates an infinitely fine grid.

Figure 6 shows a plot of the aerodynamic coefficients as the grid is made finer. Index 0 indicates the higher-order estimate of the generic value at zero grid spacing, obtained through a Richardson extrapolation from the series of lower order discrete solutions. As the grid spacing reduces, aerodynamic coefficients approach the asymptotic zero-grid spacing value, which is assumed to be close to the true numerical solution. The asymptotic value is computed using the

discrete values of the two finest grids, according to:

$$f_0 \simeq f_1 + \frac{f_1 - f_2}{\mathcal{R}^q - 1}$$

(2)

where, in the present case, f indicates the generic aerodynamic coefficient and q is the *order of convergence*, obtained using:

$$q = \ln\left(\frac{f_3 - f_2}{f_2 - f_1}\right)\frac{1}{\ln(\mathcal{R})}$$

(3)

Other useful convergence indicators are the *relative error* between grid $i + 1$ and i, $\epsilon_{i+1,i}$:

$$\epsilon_{i+1,i} = \frac{f_{i+1} - f_i}{f_i}$$

(4)

and the *Grid Convergence Index* (GCI) which indicates how much the solution would change with a further refinement of the grid. A small value of GCI indicates that the computation is within the asymptotic range, and hence further refinement would provoke negligible improvements. The GCI can be computed as:

$$\text{GCI}_{i+1,i} = F_s \frac{|\epsilon_{i+1,i}|}{\mathcal{R}^q - 1}$$

(5)

where F_s is a safety factor, recommended to be $F_s = 1.25$ for comparisons over three or more grids. It is important that each grid level yields solutions that are in the asymptotic range of convergence for the computed solution. This can be checked by observing two consecutive GCI values. If the following holds:

$$\gamma = \frac{\text{GCI}_{32}}{\text{GCI}_{21}\mathcal{R}^q} \simeq 1$$

(6)

then the solutions are in the asymptotic range of convergence. The results of the spatial convergence analysis are shown in Table 5. The reduction of *GCI* for successive grid refinements in C_L and C_D shows a good trend of convergence, while

**Table 5   Grid convergence results.**

f	$|\epsilon_{43}|$	$|\epsilon_{32}|$	$|\epsilon_{21}|$	f_0	GCI$_{43}$	GCI$_{32}$	GCI$_{21}$	γ
C_L	15.17 %	7.28 %	0.93 %	0.504423	2.79 %	1.34 %	0.17 %	1.0093
C_D	14.60 %	10.35 %	2.91 %	0.017475	6.86 %	4.86 %	1.37 %	0.9717
C_M	39.96 %	11.82 %	5.19 %	-0.003323	35.76 %	10.58 %	4.64 %	0.9507

C_M has slightly higher uncertainties. It can be concluded that the true asymptotic values are reasonably approached, at least for lift and drag. Moreover during the first ($4 \rightarrow 3$) and second ($3 \rightarrow 2$) grid refinements, there are significant

differences between the solutions f_3, f_2 and the asymptotic value f_0. However during the last step $(2 \rightarrow 1)$ this difference is considerably reduced. Hence, mesh 2 is considered the best compromise between accuracy and computational effort.

A comparison of the numerical predictions with the experimental measurements is achieved by evaluating the polars as shown in Fig. 7. Experimental and numerical values of C_L and C_D for the baseline wing are in good agreement for all the investigated angles of attack, except for the angle of attack AoA = 15°, where the wing is stalled and unsteady phenomena occur.
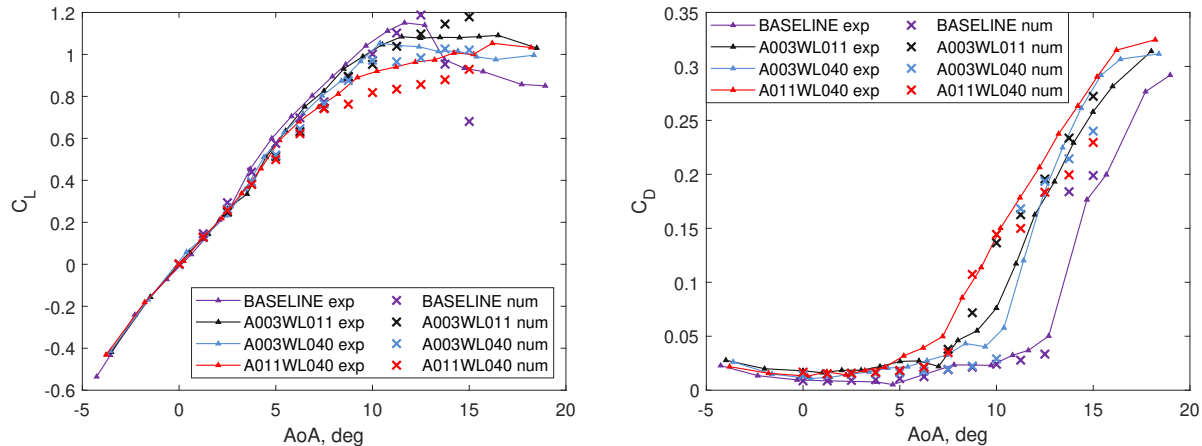
Fig. 7 Baseline and wavy leading edge wing polars: experimental data from de Paula [11] versus numerical results from CFD simulations.

Experimental and numerical values of C_L and C_D for the wavy wings are in good agreement with experimental data for the lower angles of attack, while they start to depart at approximately 10°. High angles of attack are not of interest, since the aim is to investigate ice accretion in common flight conditions. Moreover, as stated in [19], bi-periodic and complex three-dimensional effects are likely to occur at the highest angles of attack and larger span models should be used if interested in matching high AoA aerodynamic coefficients. Therefore, to the extent of this study, the angle of attack is kept below 10°.

VI. Results of icing simulations

In the following, results focus on the impact that both geometrical and environmental parameters may have on the computed collection efficiency and iced shapes. Sinusoidal amplitudes and wavelengths of the leading edge are based on the experimental geometries discussed in Section V, while environmental conditions are in the typical range encountered by aircraft and rotorcraft experiencing icing phenomena. Several differences are found between ice accretions on wavy and straight wings and possible employments of the former to reduce ice accretions are hypothesized.

A. Collection Efficiency

The convergence of the collection efficiency using a Lagrangian particle tracking approach is dependent on the number of super-cooled water droplets contained within a cloud. Consequently, a study is performed on the number of droplets to assess the independence of computed collection efficiency curves from the droplets quantity. The parameters are reported in Table 6. To address concerns of low Reynolds number flows, the subsequent collection efficiency and ice accretion simulations are performed at a slightly higher Reynolds number of $Re = 450000$. The droplets are placed $10c$ upstream in the farfield and tracked in the flow field. Droplet-droplet interactions are currently not modelled in the particle tracking computations. A wall interaction model is used to account for droplet splashing on impact. However the conditions selected are representative of Appendix-C icing conditions meaning the MVD of the droplets is low and thus splashing effects are negligible.

Table 6   Parameters for particle tracking sensitivity analysis.

| wing	$c\,[m]$	$AoA\,[°]$	Re	$MVD\,[\mu m]$	Number of particles	$\delta t\,[s]$
A003WL011	0.15	5	450000	20	0.5×10^6 to 2×10^6	1×10^{-4} to 1×10^{-5}

The sensitivity analysis is performed on a sinusoidal wing, namely the configuration A003WL011, at a constant angle of attack, $AoA = 5°$, varying the number of particles in the cloud. A single sheet of water droplets, whose normal is parallel with the chordwise direction of the wing, is used to represent the cloud. Maintaining the area of the sheet constant, the density of particles varies from 375 million particles per square meter, to 1.5 billion particles per square meter, corresponding to the absolute values of 0.5 million particles and 2 million particles, respectively. The resulting collection efficiency curves versus non-dimensionalized curvilinear coordinate at the peak, trough and mid spanwise sections of the wing are displayed in Fig. 8.

Increasing the particle density, the collection efficiency curves are progressively smoothed and they finally approach a common trend in the last refinement step. Hence, a particle density of 750 million particles per square meter is used to compute the total number of particles in the clouds and it corresponds to approximately 1 million particles for the lower span configuration, A003WL011, while almost 3.6 million particles for the baseline wing and A003WL040 and A011WL040 sinusoidal wings.

As for the integration time step used in the forward Euler algorithm, a value of $\delta t = 2 \times 10^{-5} s$ is chosen as the best compromise between accuracy and computational speed as shown in Fig. 9.

Results of the particle tracking phase on the wings with wavy leading edges are summarized in Figs. 10 & 11. The results show the collection efficiency, β, comparison among the baseline and the wavy wings, for a given cloud and the same flow conditions at AoA = 5° and MVD = $20\mu m$.

The three-dimensional collection efficiency distributions are displayed in Fig. 10. The three-dimensional effects
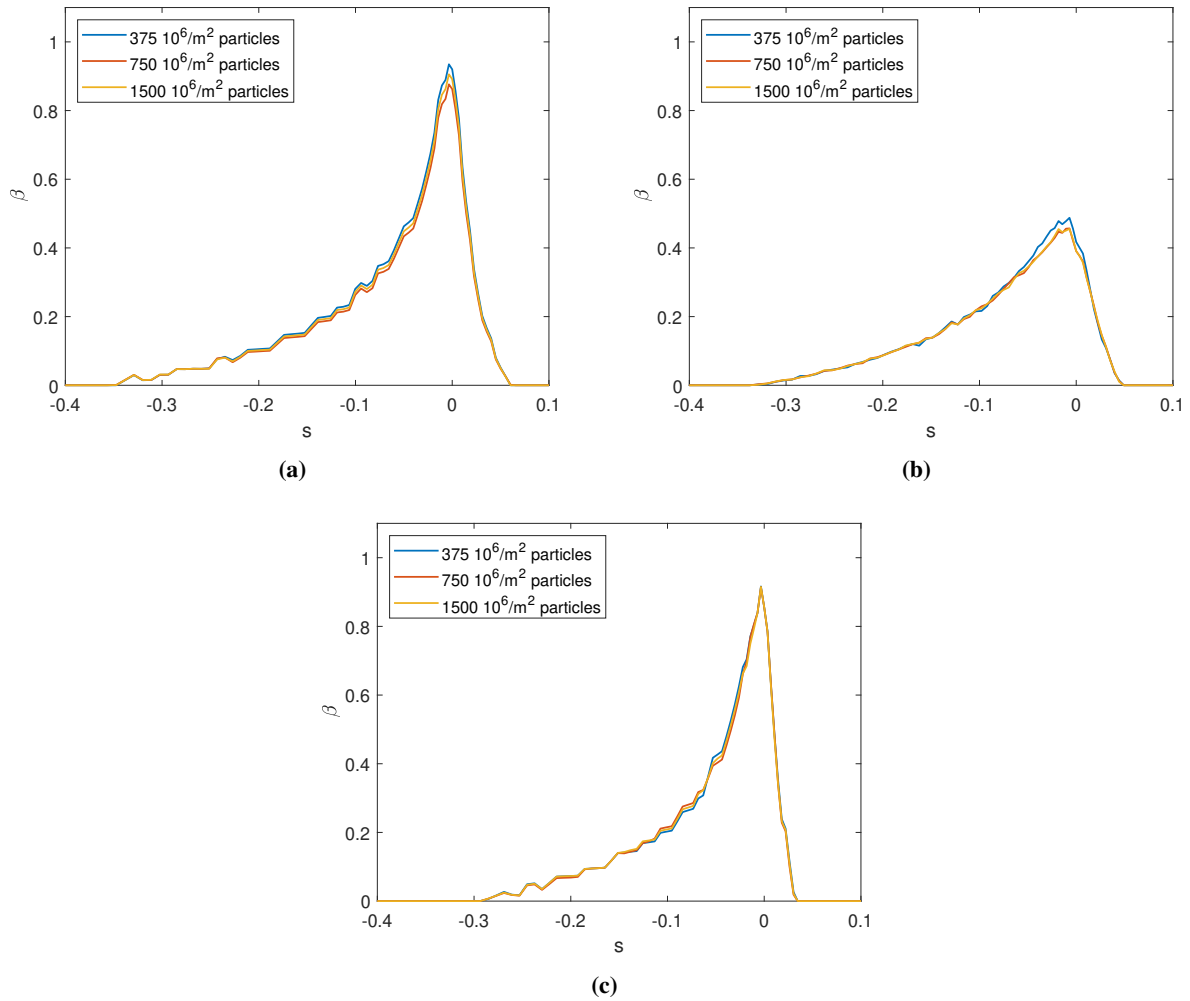
Fig. 8   Particle sensitivity analysis performed on the sinusoidal leading edge wing A003WL011 at $AoA = 5°$. Spanwise section: (a) peak, (b) mid, (c) trough.

induced in the flow field around the leading edge by the wavy geometry have a major role in influencing the collection efficiency, β. The latter assumes its maximum value in the proximity of peaks and troughs, where the flow stagnates, and generally has magnitudes close to the baseline configuration. However, on the remaining portions of the leading edge, the collection efficiency is lower than at a corresponding spanwise location of the baseline, especially at sections halfway peaks and troughs, referred to as mid sections in the following.

The collection efficiency at mid sections is reduced due to the complex shape of the leading edge which produces a three-dimensional flow field that tends to deviate particles from the wing surface, reducing the possibility of impact.

The two-dimensional collection efficiency distributions are displayed in Fig. 11. The resulting collection efficiency distribution is qualitatively the same for all configurations but the reduction at mid sections is found to be directly proportional to the sine amplitude of the leading edge and inversely proportional to its wavelength: higher sine

17
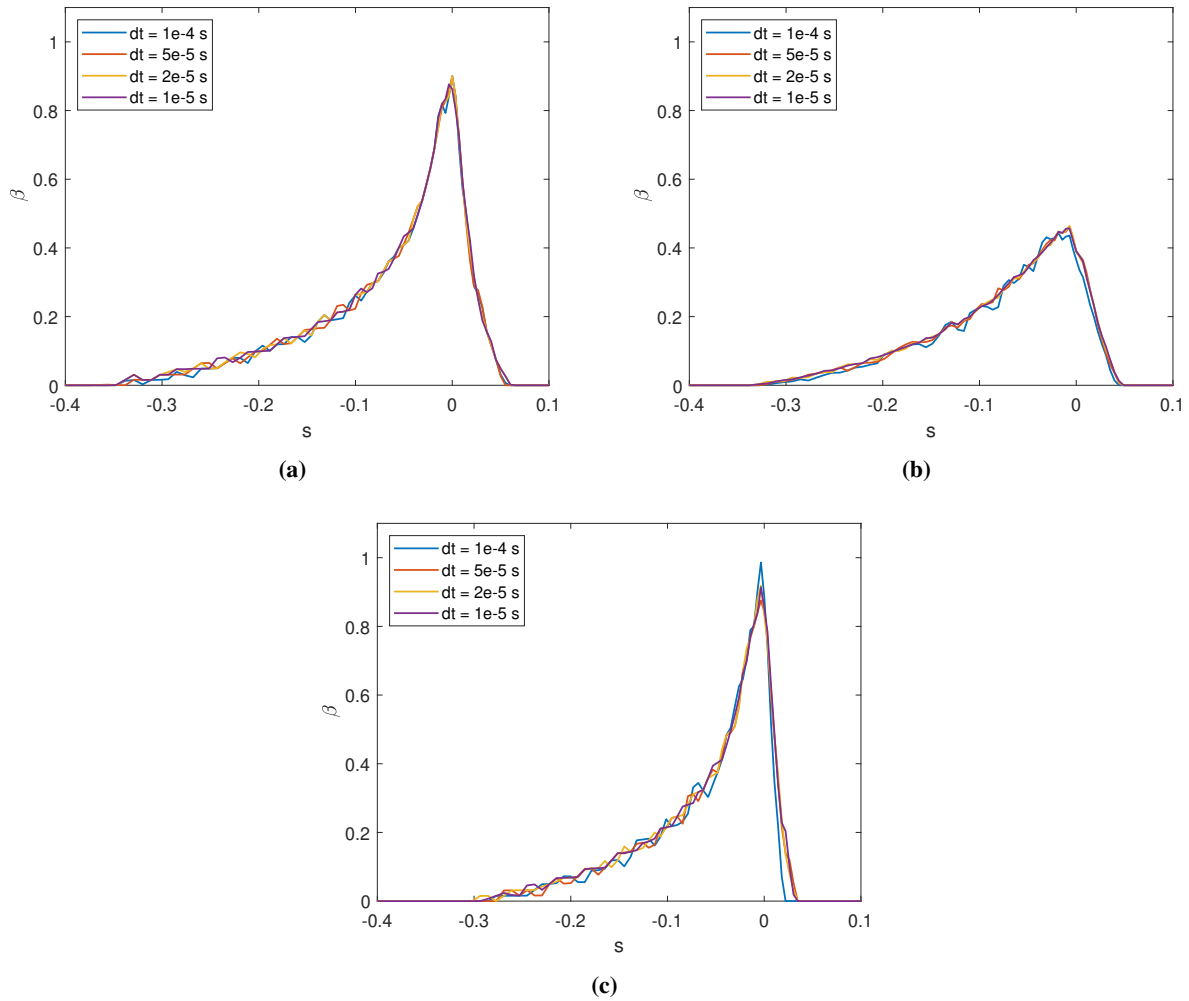
Fig. 9 Integration time step sensitivity analysis performed on the sinusoidal leading edge wing A003WL011 at $AoA = 5°$. Spanwise section: (a) peak, (b) mid, (c) trough.

amplitudes or lower wavelengths reduce the collection efficiency at the leading edge between peaks and troughs. That is the reason why configurations A003WL011 and A011WL040 present a much higher β reduction at mid sections (more than 50% lower than those at a corresponding baseline's location) than A003WL040.

Moreover, parametric analysis varying AoA and MVD are performed as well. Results show how the former parameter has only negligible effects on the 3D collection efficiency distribution. On the other hand, the latter greatly influences the β value at mid sections: lower MVD reduces the number of water droplet impacts on the surface, thus leading to reduced ice accretions there. The physical explanation is that smaller droplets are subject to increasing aerodynamic forces, hence the spanwise flow can deviate most of them, preventing impacts on the surface. On the other hand, trajectories of larger droplets are less affected by the surrounding flow direction because of increasing inertia forces. As a result, the larger droplets move along straighter trajectories, eventually impacting the surface. The effect of

18
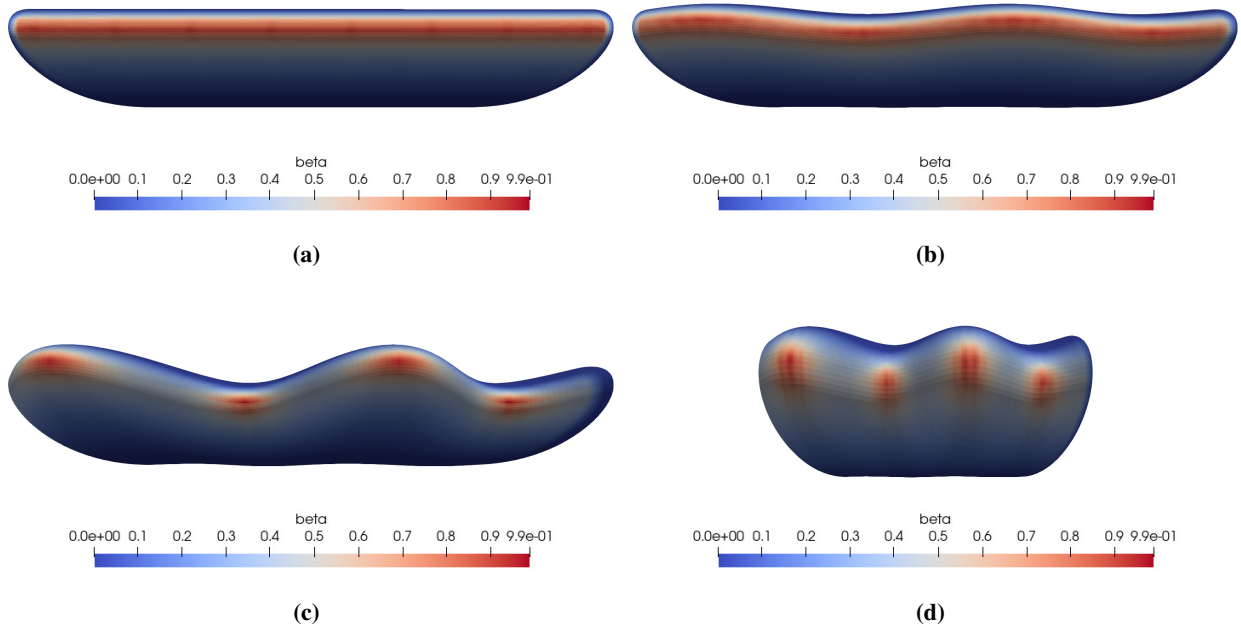
Fig. 10 Collection efficiency at AoA = 5°. (a) Baseline, (b) A003WL040, (c) A011WL040, (d) A003WL011.
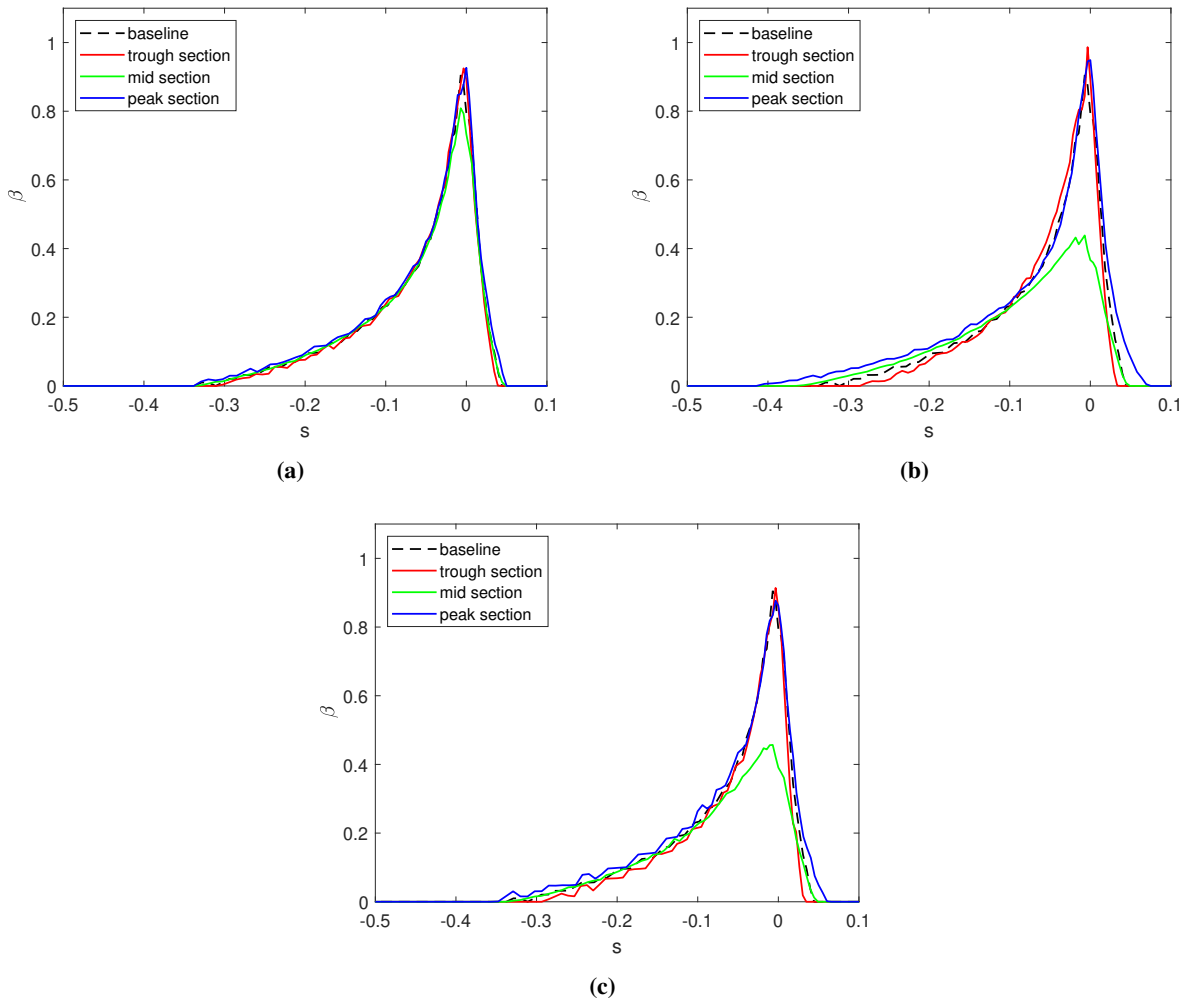
Fig. 11 Collection efficiency distribution at AoA = 5°. (a) A003WL040, (b) A011WL040, (c) A003WL011.

MVD on the collection efficiency is shown in Fig. 12 where only the wavy configuration A011WL040 is reported and compared to the baseline. Below a certain threshold of MVD, almost all water droplets impacts are prevented on mid sections of the wavy wing, thus nearly eliminating ice accretion on those regions of the leading edge.
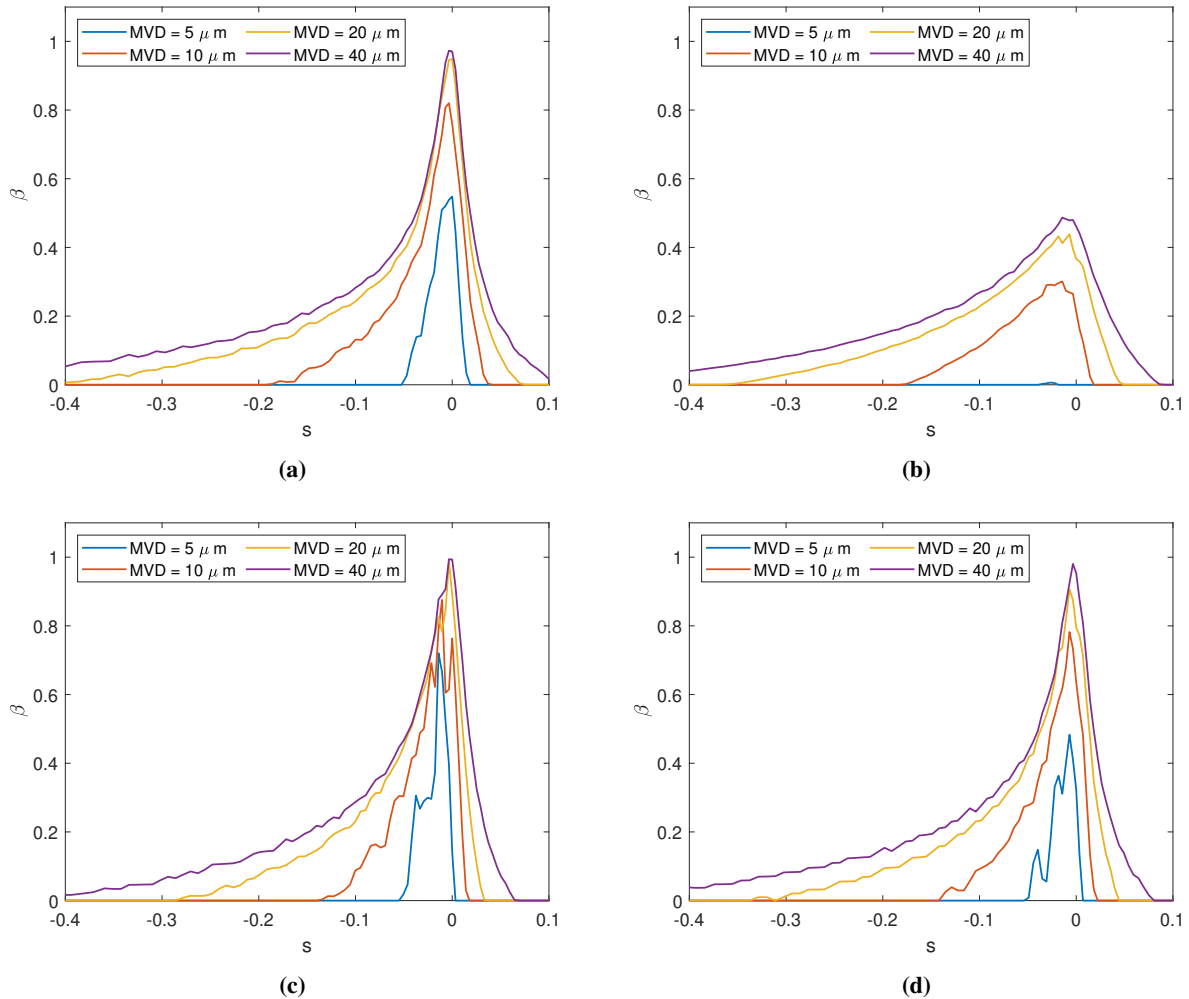
Fig. 12   Effect of Median Volume Diameter, MVD, on the collection efficiency. Results reported for configuration A011WL040 at AoA = 5°. (a) A011WL040 peak, (b) mid, (c) trough, (d) baseline mid.

B. Ice Accretion

The three-dimensional ice accretion simulations use the multi-step structure as shown in Fig. 2. The ice accretion simulations focus on the A011WL040 configuration due to the three-dimensional effects being most prevalent. Numerical tests are conducted in both the rime and glaze icing regime.

Environmental icing conditions are reported in Table 7 and 8. The environmental conditions are maintained constant with the sole exception of outside air temperature, which is chosen to be $T = -10°C$ or $T = -5°C$. The lower temperatures reflect the rime ice regime, while the higher temperatures are representative of the glaze ice regime.

An accretion period of 210 seconds is chosen for rime ice. Between one icing iteration and the subsequent one, a time interval, Δt, of 30 seconds is considered: for such time step, the ice layer which forms on the wing's surface is believed to be high enough to provoke appreciable differences in the wing's shape, at the same time without totally upsetting the particles' trajectories and the resultant collection efficiency.

Table 7   Parameters for multi-step icing simulations in rime regime.

AoA[°]	Re	$U_\infty[m/s]$	$T[K]$	$p[Pa]$	MVD[μm]	LWC[g/m^3]	$\Delta t[s]$	$time[s]$
5	450000	61	263.15	61808.25	20	0.6	30	210

Table 8   Parameters for multi-step icing simulations in glaze regime.

| AoA[°]	Re	$U_\infty[m/s]$	$T[K]$	$p[Pa]$	MVD[μm]	LWC[g/m^3]	$\Delta t[s]$	$time[s]$
5	450000	61	268.15	61808.25	20	0.6	30	90, 180

Figure 13 shows the progression of the ice front as time evolves across the three notable spanwise sections for the wavy wing. Also, the iced mid section from the straight NACA0012 is reported for comparison.

As typical of rime ice, the iced shapes present a certain smoothness, both for the baseline and the sinusoidal leading edge, where ice forms more or less streamlined accretions. The main difference is represented by the reduced accretion of ice on wavy wing mid sections, directly related the variation of the collection efficiency.

The loss of aerodynamic performance is comparable for both wings: the iced baseline presents a 9.7% reduction in lift and 37.9% increment in drag with respect to the clean geometry, while for the wavy wing an 8.3% reduction in lift and 29.5% increment in drag are observed. However it must be noted that the resultant values of aerodynamic coefficients do not account for the increased surface roughness due to the ice accretion, hence they are not believed to be a precise estimate of the real ones, especially for what regards drag. Also, as for the clean geometries, absolute values of lift and drag for the iced wavy wing are still respectively lower and higher than those for the iced straight wing, showing how aerodynamic performances of a straight leading edge are still superior. Finally, the three-dimensional iced shapes of both the wavy and straight wings are compared in Fig. 14.

Glaze icing simulations, on the other hand, are much more challenging from the CFD point of view. The formation of the typical horns at the leading edge introduces sharp discontinuities at the surface. The meshing of such regions is inevitably of poor quality, leading the simulations to diverge when accretions overcome a certain threshold. In the present work the final time of accretion has been of only 90 seconds for the baseline wing.

Conversely, for the wavy geometry an accretion time of 180 seconds is reached, and the resultant iced shape shows interesting effects, as illustrated in Fig. 15 and Fig. 16, respectively showing the bi-dimensional accretions on notable spanwise stations and the three-dimensional iced shapes of both the straight and the wavy wings. Figure 16 illustrates

21
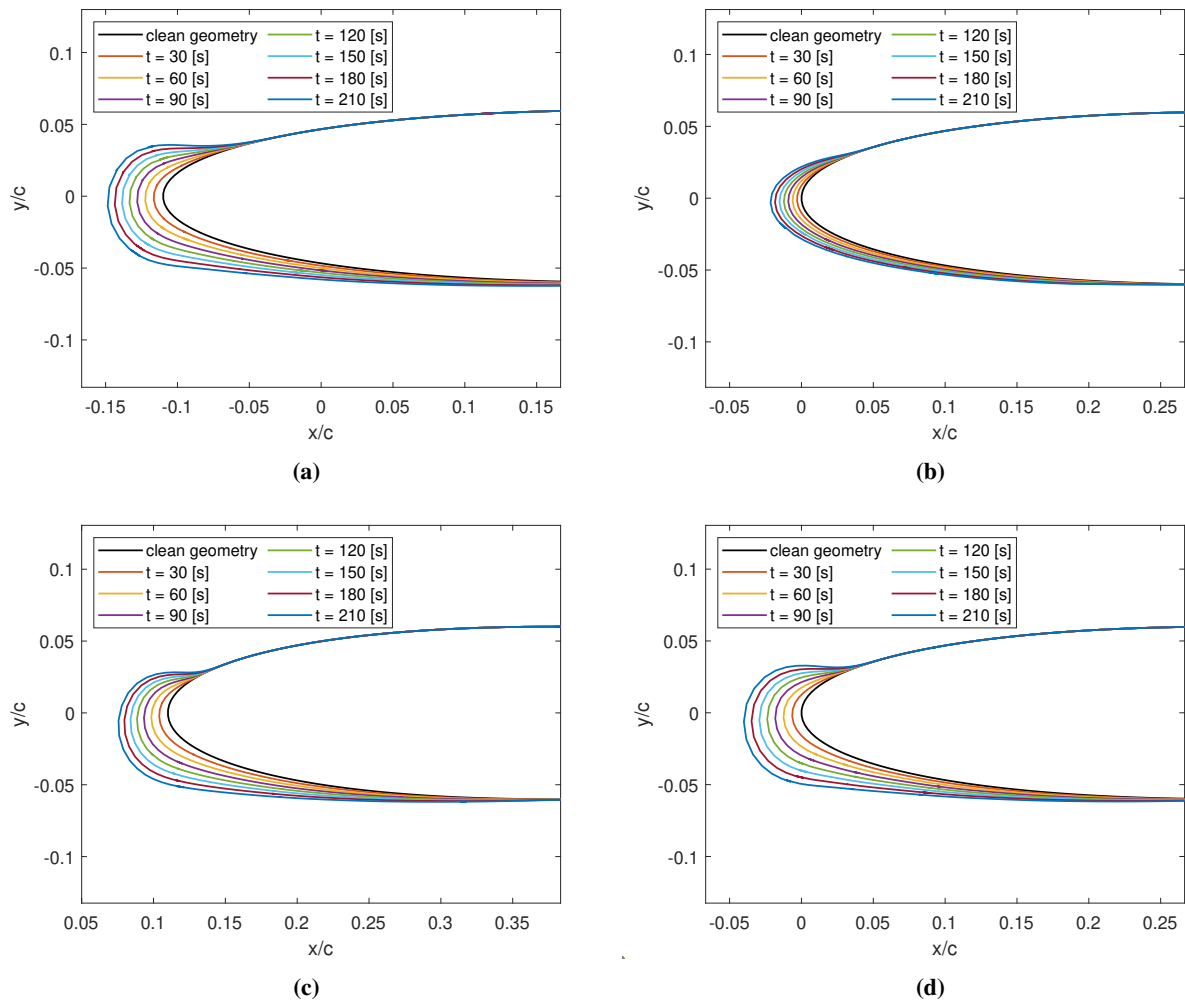
Fig. 13   Multi-step icing during rime conditions. Ice shapes for A011WL040 (a) peak, (b) mid, (c) trough, (d) baseline are reported in the normal direction to the clean wing surface.
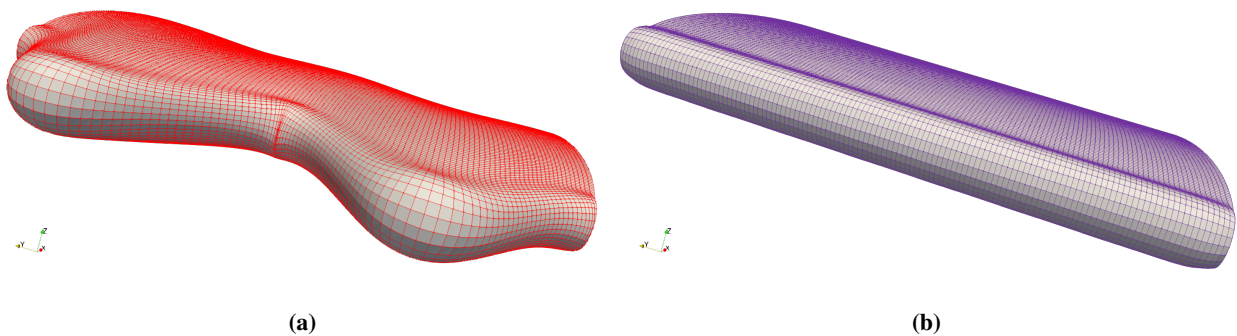
Fig. 14   Three-dimensional rime ice shapes for (a) A011WL040 and (b) baseline wing after 210 **s.**
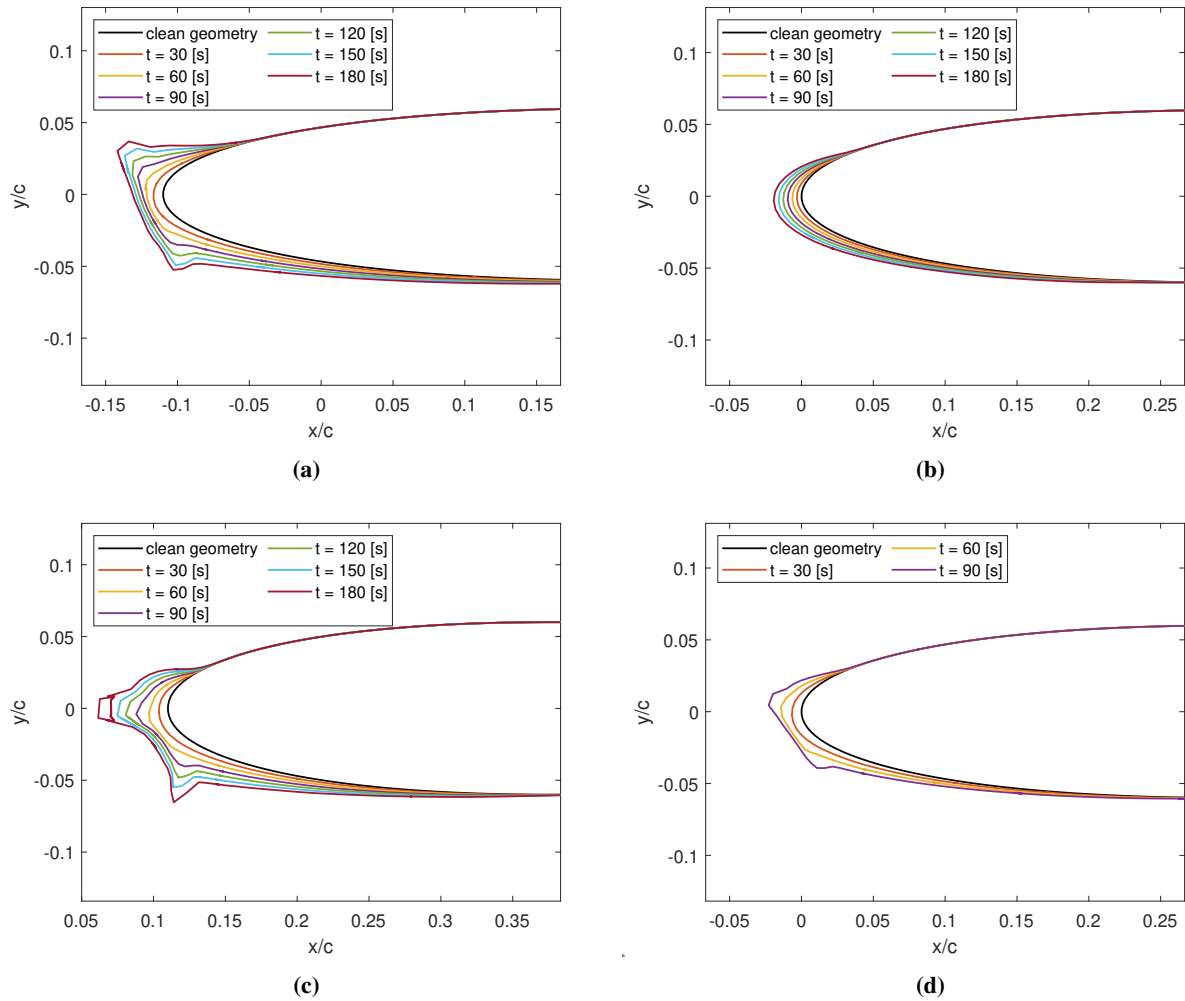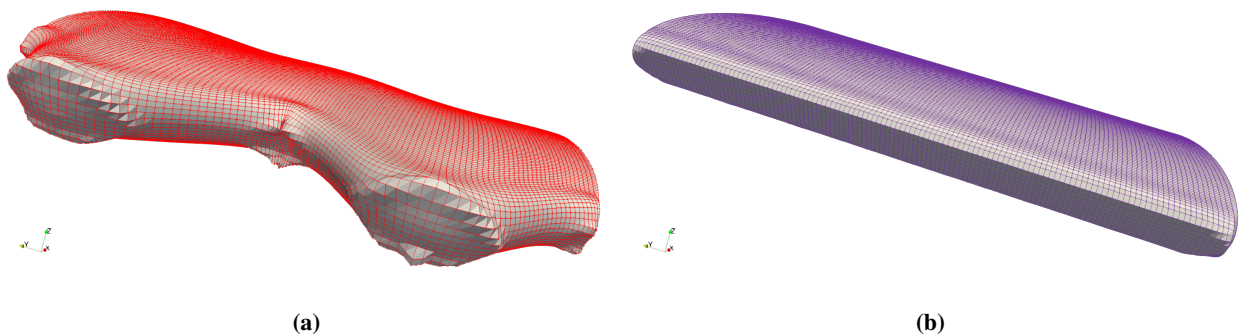
Fig. 15 Multi-step icing during glaze conditions. Ice shapes for A011WL040 (a) peak, (b) mid, (c) trough, (d) baseline are reported in the normal direction to the clean wing surface.

Fig. 16 Three-dimensional glaze ice shapes for (a) A011WL040 and (b) baseline wing after 180 s **and** 90 s, **respectively.**

how in the trough section of A011WL040 ice fronts collide, leading to an un-physical interpenetration at the last time step. Also, it is very interesting to note how on the wavy wing, glaze ice predominantly occurs only in the proximity of leading edge's peaks and troughs.

In both areas, the water film freezes after having spread in multiple directions, driven by the wall shear stress. However the effect in resultant geometry is different: at trough spanwise sections, the concavity of the wing surface is increased by the formation of ice horns on the suction and pressure sides of the wing, which, together with the lateral naturally inclined portions of the leading edge, concur to the formation of a three-dimensional cavity. Also, the shear stress at the surface causes an additional inflow of water from the lateral neighbouring areas, which finally freezes resulting in increased horns dimensions, with respect to those at peak sections.

On the other hand, the ice layer at peaks results in a more flattened geometry of the leading edge, as the liquid film is also driven by the shear stress towards lateral positions, where it freezes leading to the formation of characteristic *lateral ice horns*.

Finally, the more streamlined geometric shape at mid sections indicates the formation of rime ice structures, confirming that glaze ice difficultly occurs in those portions of the leading edge.

The loss of performances after an icing period of 60 seconds at the new conditions is represented by a 3.9% reduction in lift and 8.8% increase in drag for the baseline, while the wavy wing presents a 1.8% reduction in lift and 3.5% increase in drag. The resultant absolute values of lift and drag for the different wings approach common values after the accretion period. Therefore, the formation of glaze ice in isolated portions of the leading edge provokes a reduced loss of performances. Hypothetically, for longer accretion periods and environmental conditions promoting glaze icing, performances of the wavy wing may overcome those of the straight one.

VII. Conclusions

This work aimed to study the ice accretion on wings with a sinusoidal leading edge. The icing simulation is split in three sequential steps: the computation of the aerodynamic quantities over the clean geometry, the water droplets trajectories computation, and finally the estimation of the ice accretion for a certain exposure time, with the associated re-meshing of the iced geometry. CFD simulations over the clean geometries are compared with experimental results published in the open literature and show a good match between the numerical flow field and experimental visualizations. Also, aerodynamic coefficients are in good agreement with experiments at low AoA. However, the clean wavy leading edge experiments and simulations were performed at low Re. The aerodynamic influence of wavy leading edges should be further investigated at higher Re conditions which are more representative of in-flight icing. The particle tracking phase is then performed and a comparison among the baseline wing and the sinusoidal leading edge ones show how the latter present a considerable reduction of collection efficiency in regions that are halfway the leading edge's peaks and troughs, without appreciably increasing the magnitude on the remaining portions of the leading edge. The reduction in

the collection efficiency at highlighted portions of the wavy leading edges has a direct correlation with the ice shapes of wavy leading edge wings. It is shown how for wavy wings, at mild temperatures, glaze ice formation is delayed at mid sections between leading edge peaks and troughs. The absence of glaze ice for the given accretion period is a direct consequence of the reduced collection efficiency in those leading edge portions. As a consequence, only rime ice grows on mid sections, while glaze ice forms elsewhere. Finally, the formation of glaze ice on isolated portions of the leading edge results in a reduced loss of aerodynamic performances of the wavy wings with respect to the straight counterpart. However, this behaviour should be further investigated with additional analysis, since the low icing period tested in this work is only sufficient to establish a possible trend. Additionally, the presence of colliding ice fronts on the wavy leading edges during long exposure times is shown to be an issue. In conclusion, the icing mechanism on wavy wings is in many ways similar to the one on straight wings in rime regime, but presents some peculiar differences due to the characteristic geometric shape when glaze ice occurs.

References

[1] Gent, R. W., Dart, N. P., and Cansdale, J. T., "Aircraft icing," *Philosophical Transactions of the Royal Society of London. Series A: Mathematical, Physical and Engineering Sciences*, Vol. 358, No. 1776, 2000, pp. 2873–2911. https://doi.org/10.1098/rsta.2000.0689, URL https://royalsocietypublishing.org/doi/10.1098/rsta.2000.0689.

[2] Lynch, F. T., and Khodadoust, A., "Effects of ice accretions on aircraft aerodynamics," *Progress in Aerospace Sciences*, Vol. 37, No. 8, 2001, pp. 669–767. https://doi.org/10.1016/S0376-0421(01)00018-5, URL https://www.sciencedirect.com/science/article/abs/pii/S0376042101000185.

[3] Baars, W. J., Stearman, R. O., and Tinney, C. E., "A Review on the Impact of Icing on Aircraft Stability and Control," *Journal of Aeroelasticity and Structural Dynamics*, Vol. 2, No. 1, 2010. https://doi.org/doi:10.3293/asdj.2010.7.

[4] Lou, D., and Hammond, D. W., "Heat and mass transfer for ice particle ingestion inside aero-engine," *Journal of turbomachinery*, Vol. 133, No. 3, 2011. https://doi.org/10.1115/1.4002419.

[5] Jäckel, R., Gutiérrez-Urueta, G., and Tapia, F., "A review on Pitot tube icing in aeronautics: Research-design and characterization–future trends," *Flow Measurement and Instrumentation*, Vol. 81, 2021, p. 102033. https://doi.org/10.1016/j.flowmeasinst.2021.102033, URL https://www.sciencedirect.com/science/article/abs/pii/S0955598621001394.

[6] Llamas Sandin, R. C., "Aircraft tail surface with a leading edge section of undulated shape," , 29 July 2014. URL https://patents.google.com/patent/US8789793B2/en, patent No. US 8,789,793 B2.

[7] Hansen, K. L., Kelso, R. M., and Dally, B. B., "Performance variations of leading-edge tubercles for distinct airfoil profiles," *AIAA journal*, Vol. 49, No. 1, 2011, pp. 185–194. https://doi.org/10.2514/1.J050631, URL https://arc.aiaa.org/doi/10.2514/1.J050631.

[8] Johari, H., Henoch, C., Custodio, D., and Levshin, A., "Effects of leading-edge protuberances on airfoil performance," *AIAA Journal*, Vol. 45, No. 11, 2007, pp. 2634–2642. https://doi.org/10.2514/1.28497, URL https://arc.aiaa.org/doi/10.2514/1.28497.

[9] Weber, P. W., Howle, L. E., Murray, M. M., and Miklosovic, D. S., "Computational evaluation of the performance of lifting surfaces with leading-edge protuberances," *Journal of Aircraft*, Vol. 48, No. 2, 2011, pp. 591–600. https://doi.org/10.2514/1.C031163, URL https://arc.aiaa.org/doi/10.2514/1.C031163.

[10] Butt, F. R., and Talha, T., "Numerical investigation of the effect of leading-edge tubercles on propeller performance," *Journal of Aircraft*, Vol. 56, No. 3, 2019, pp. 1014–1028. https://doi.org/10.2514/1.C034845, URL https://arc.aiaa.org/doi/full/10.2514/1.C034845.

[11] Agrico de Paula, A., "The airfoil thickness effects on wavy leading edge phenomena at low Reynolds number regime." Ph.D. thesis, Universidade de São Paulo, 2016. https://doi.org/10.11606/T.3.2016.tde-27092016-153422.

[12] Malipeddi, A. K., Mahmoudnejad, N., and Hoffmann, K. A., "Numerical analysis of effects of leading-edge protuberances on aircraft wing performance," *Journal of Aircraft*, Vol. 49, No. 5, 2012, pp. 1336–1344. https://doi.org/10.2514/1.C031670, URL https://arc.aiaa.org/doi/10.2514/1.C031670.

[13] Ng, B. F., New, T. H. D., and Palacios, R., "Effects of leading-edge tubercles on wing flutter speeds," *Bioinspiration & biomimetics*, Vol. 11, No. 3, 2016, p. 036003. https://doi.org/10.1088/1748-3190/11/3/036003, URL https://iopscience.iop.org/article/10.1088/1748-3190/11/3/036003.

[14] New, D. T. H., and Ng, B. F., *Flow Control Through Bio-inspired Leading-Edge Tubercles: Morphology, Aerodynamics, Hydrodynamics and Applications*, 1st ed., Springer, Cham, 2020. https://doi.org/10.1007/978-3-030-23792-9, URL https://link.springer.com/book/10.1007/978-3-030-23792-9, ISBN: 978-3-030-23792-9.

[15] Fish, F. E., and Battle, J. M., "Hydrodynamic design of the humpback whale flipper," *Journal of Morphology*, Vol. 225, No. 1, 1995, pp. 51–60. https://doi.org/10.1002/jmor.1052250105, URL https://onlinelibrary.wiley.com/doi/abs/10.1002/jmor.1052250105.

[16] Gopinathan, V., and Rose, J. B. R., "Aerodynamics with state-of-the-art bioinspired technology: Tubercles of humpback whale," *Proceedings of the Institution of Mechanical Engineers, Part G: Journal of Aerospace Engineering*, Vol. 235, No. 16, 2021, pp. 2359–2377. https://doi.org/10.1177/09544100211001501, URL https://journals.sagepub.com/doi/abs/10.1177/09544100211001501.

[17] Hansen, K. L., Rostamzadeh, N., Kelso, R. M., and Dally, B. B., "Evolution of the streamwise vortices generated between leading edge tubercles," *Journal of Fluid Mechanics*, Vol. 788, 2016, pp. 730–766. https://doi.org/doi:10.1017/jfm.2015.611.

[18] Skillen, A., Revell, A., Pinelli, A., Piomelli, U., and Favier, J., "Flow over a wing with leading-edge undulations," *AIAA Journal*, Vol. 53, No. 2, 2015, pp. 464–472. https://doi.org/10.2514/1.J053142, URL https://arc.aiaa.org/doi/10.2514/1.J053142.

[19] Rostamzadeh, N., Hansen, K., Kelso, R., and Dally, B., "The formation mechanism and impact of streamwise vortices on NACA 0021 airfoil's performance with undulating leading edge modification," *Physics of Fluids*, Vol. 26, No. 10, 2014, p. 107101. https://doi.org/10.1063/1.4896748, URL https://aip.scitation.org/doi/10.1063/1.4896748.

[20] Yasuda, T., Fukui, K., Matsuo, K., Minagawa, H., and Kurimoto, R., "Effect of the Reynolds Number on the Performance of a NACA0012 Wing with Leading Edge Protuberance at Low Reynolds Numbers," *Flow, Turbulence and Combustion*, Vol. 102, No. 2, 2019, pp. 435–455. https://doi.org/10.1007/s10494-018-9978-3, URL https://link.springer.com/article/10.1007/s10494-018-9978-3.

[21] Broeren, A., "1st AIAA Ice Prediction Workshop," Workshop in conjunction with the AIAA AVIATION FORUM 2021, 26-29 June 2021. URL https://icepredictionworkshop.wordpress.com, virtual Event.

[22] Xi, C., and Qi-Jun, Z., "Numerical Simulations for Ice Accretion on Rotors Using New Three-Dimensional Icing Model," *Journal of Aircraft*, Vol. 54, No. 4, 2017, pp. 1428–1442. https://doi.org/10.2514/1.C033986, URL https://doi.org/10.2514/1.C033986.

[23] Chen, X., and Zhao, Q.-J., "Computational Investigations of Water Collection Efficiency on Blades in Unsteady Vortex Flowfield of Rotor," *Aerospace Science and Technology*, Vol. 79, 2018, pp. 482–491.

[24] Lavoie, P., Radenac, E., Blanchard, G., Laurendeau, E., and Villedieu, P., "Immersed Boundary Methodology for Multistep Ice Accretion Using a Level Set," Journal of Aircraft, Published Online: 11 Jan 2022. https://doi.org/10.2514/1.C036492, URL https://doi.org/10.2514/1.C036492.

[25] Szilder, K., and Lozowski, E. P., "Comparing Experimental Ice Accretions on a Swept Wing with 3D Morphogenetic Simulations," *Journal of Aircraft*, Vol. 55, No. 6, 2018, pp. 2546–2549. https://doi.org/10.2514/1.C034879, URL https://doi.org/10.2514/1.C034879.

[26] Gori, G., Congedo, P. M., Le Maître, O., Bellosta, T., and Guardone, A., "Modeling In-Flight Ice Accretion Under Uncertain Conditions," Journal of Aircraft, Published Online: 30 Nov 2021. https://doi.org/10.2514/1.C036545, URL https://doi.org/10.2514/1.C036545.

[27] Gori, G., Zocca, M., Garabelli, M., Guardone, A., and Quaranta, G., "PoliMIce: A simulation framework for three-dimensional ice accretion," *Applied Mathematics and Computation*, Vol. 267, 2015, pp. 96–107. https://doi.org/10.1016/j.amc.2015.05.081, URL https://www.sciencedirect.com/science/article/abs/pii/S0096300315007055.

[28] Morelli, M., "Simulation and Detection of Ice Formation and Shedding on Rotorcraft," Ph.D. thesis, Politecnico di Milano, February 2021. URL http://hdl.handle.net/10589/170615.

[29] Morelli, M., and Guardone, A., "A simulation framework for rotorcraft ice accretion and shedding," *Aerospace Science and Technology*, 2021, p. 107157. https://doi.org/10.1016/j.ast.2021.107157, URL https://www.sciencedirect.com/science/article/abs/pii/S1270963821006672, article in press.

[30] Morelli, M., Zhou, B. Y., and Guardone, A., "Acoustic Characterization of Glaze and Rime Ice Structures on an Oscillating Airfoil via Fully Unsteady Simulations," *Journal of the American Helicopter Society*, Vol. 65, No. 4, 2020, pp. 1–12. https://doi.org/10.4050/JAHS.65.042004, URL https://www.ingentaconnect.com/content/ahs/jahs/2020/00000065/00000004/art00004.

[31] Palacios, F., Economon, T. D., Aranake, A., Copeland, S. R., Lonkar, A. K., Lukaczyk, T. W., Manosalvas, D. E., Naik, K. R., Padron, S., Tracey, B., Variyar, A., and Alonso, J. J., "Stanford university unstructured (SU2): Analysis and design technology for turbulent flows," *52nd Aerospace Sciences Meeting*, National Harbor, Maryland, 13-17 January, 2014, p. 0243. https://doi.org/10.2514/6.2014-0243, URL https://arc.aiaa.org/doi/10.2514/6.2014-0243.

[32] Bellosta, T., Parma, G., and Guardone, A., "A robust 3D particle tracking solver for in-flight ice accretion using arbitrary precision arithmetic," *COUPLED VIII: proceedings of the VIII International Conference on Computational Methods for Coupled Problems in Science and Engineering*, Sitges, Barcelona, Spain, 3-5 June, 2019, pp. 622–633. URL http://hdl.handle.net/2117/190171.

[33] Myers, T. G., "Extension to the Messinger model for aircraft icing," *AIAA Journal*, Vol. 39, No. 2, 2001, pp. 211–218. https://doi.org/10.2514/2.1312, URL https://arc.aiaa.org/doi/10.2514/2.1312.

[34] Gori, G., Parma, G., Zocca, M., and Guardone, A., "Local solution to the unsteady Stefan problem for in-flight ice accretion modeling," *Journal of Aircraft*, Vol. 55, No. 1, 2018, pp. 251–262. https://doi.org/10.2514/1.C034412, URL https://arc.aiaa.org/doi/10.2514/1.C034412.

[35] Morelli, M., Bellosta, T., and Guardone, A., "Efficient radial basis function mesh deformation methods for aircraft icing," *Journal of Computational and Applied Mathematics*, Vol. 392, 2021, p. 113492. https://doi.org/10.1016/j.cam.2021.113492, URL https://www.sciencedirect.com/science/article/pii/S0377042721001114.

[36] Papadakis, M., Hung, K. E., Vu, G. T., Yeong, H. W., Bidwell, C. S., Breer, M. D., and Bencic, T. J., "Experimental Investigation of Water Droplet Impingement on Airfoils, Finite Wings, and an S-Duct Engine Inlet," National Aeronautics and Space Administration, Glenn Research Center, Technical Memorandum No. 2002-211700, October 2002.

[37] Lee, S., Broeren, A. P., Kreeger, R. E., Potapczuk, M. G., and Utt, L., "Implementation and validation of 3-D ice accretion measurement methodology," *6th AIAA Atmospheric and Space Environments Conference*, Atlanta, GA, USA, 16-20 June, 2014, p. 2613. Https://doi.org/10.2514/6.2014-2613.

[38] Beretta, L., "A numerical study of the ice accretion over sinusoidal leading edge wings," Master's thesis, Politecnico di Milano, 2021. URL http://hdl.handle.net/10589/174075.

[39] Roache, P. J., "Quantification of uncertainty in computational fluid dynamics," *Annual Review of Fluid Mechanics*, Vol. 29, No. 1, 1997, pp. 123–160. https://doi.org/10.1146/annurev.fluid.29.1.123, URL https://www.annualreviews.org/doi/10.1146/annurev.fluid.29.1.123.